Modeling the Influence of Process Parameters and Additional Heat Sources on Residual Stresses in Laser Cladding

F. Brückner, D. Lepski, and E. Beyer

In laser cladding thermal contraction of the initially liquid coating during cooling causes residual stresses and possibly cracks. Preweld or postweld heating using inductors can reduce the thermal strain difference between coating and substrate and thus reduce the resulting stress. The aim of this work is to better understand the influence of various thermometallurgical and mechanical phenomena on stress evolution and to optimize the induction-assisted laser cladding process to get crack-free coatings of hard materials at high feed rates. First, an analytical one-dimensional model is used to visualize the most important features of stress evolution for a Stellite coating on a steel substrate. For more accurate studies, laser cladding is simulated including the powder-beam interaction, the powder catchment by the melt pool, and the self-consistent calculation of temperature field and bead shape. A three-dimensional finite element model and the required equivalent heat sources are derived from the results and used for the transient thermomechanical analysis, taking into account phase transformations and the elastic-plastic material behavior with strain hardening. Results are presented for the influence of process parameters such as feed rate, heat input, and inductor size on the residual stresses at a single bead of Stellite coatings on steel.

1. Introduction

Laser cladding is increasingly used for the generation of corrosion- and wear-protective coatings and for the repair of tools and components. It is able to yield a strong interfacial bond between the substrate and the coating without significant dilution of one material into the other.

In the laser cladding process, the pulverized coating material is transported by a carrier gas through a nozzle onto the workpiece surface (Fig. 1). There it penetrates into the melt pool that is generated by the laser beam on the moving substrate. Care must be taken to adjust the temperature field so that a strong metallurgical bond between the deposit and the substrate is achieved with very low dilution of the coating with substrate material.

Since the coating material is in the liquid state while being deposited on the cold substrate, thermal contraction of the deposit unavoidably leads to the evolution of

residual stresses and workpiece distortion. Residual stresses in wear- or corrosion-protective coatings may strongly influence mechanical properties such as wear and fatigue resistance and fracture strain. Residual stresses enhance the danger of cracking or delamination of such coatings either during the cladding process itself or later during external loading. Many high-strength materials as some nickel- or cobalt-base alloys may yield coatings of large hardness and wear resistance but are rather sensitive to cracking. Therefore, it is very difficult to get crack-free wear-resistant coatings on steel substrates with a hardness of more than about 50 HRC.

Residual stresses depend on process parameters such as heating and cooling rates as well as on the thermo-physical and other material properties, especially on the thermal expansion coefficients, the elastic-plastic behavior, and the occurring phase transformations. Therefore, residual stresses and the related danger of cracking may be influenced by an appropriate handling of the cladding process.

Simulation of the cladding process and of the related stress evolution is becoming an increasingly important tool to better understand these phenomena, to determine those process parameter values that yield the required results of treatment, and to derive methods to reduce stress and distortion.

2. State of the Art

The history of laser cladding simulation started before 1990. Pioneers in this field were Weerasinghe and Steen (Ref 1) who in 1983 developed a three-dimensional finite

F. Brückner and **E. Beyer,** Institute for Surface Technology and Production Metrology IOF, Dresden University of Technology, Dresden, Germany; **D. Lepski** and **E. Beyer,** Fraunhofer Institute for Material and Beam Technology IWS, Dresden, Germany. Contact e-mail: Frank.Brueckner@iws.fraunhofer.de.

Nomenclature

Symbol	Quantity
a, mm^2/s	Heat diffusivity
aa, mm	Ellipsoid half axis (x-direction)
bb, mm	Ellipsoid half axis (y-direction)
cc, mm	Ellipsoid half axis (z-direction)
b, mm	Characteristic length of the bead cross section
c, c_P, Ws/(g K)	Specific heat, specific heat of powder particles
d, mm	Thickness of coating
$\vec{e}_x$, $\vec{e}_z$	Unit vector along the x-direction, z-direction
erfc(x)	Complementary error function $\frac{2}{\sqrt{\pi}} \int_x^\infty dx' \exp\left(-x'^2\right)$
$f(x, y, z; \alpha_C)$	Bead shape function
$\vec{g} = -g\vec{e}_z$, mm/s^2	Gravity acceleration vector
h, mm	Substrate plate thickness
$h_P(x, y, z; R)$, Ws/g	Specific enthalpy of particle with radius R at position (x, y, z)
ierfc(x)	Integrated complementary error function $\int_x^\infty dx'\, erfc(x')$
$j(x, y, z)$, g/(s mm^2),	Mass flow density
$j^*(x, y, z)$, g/(s mm^2)	Mass flow density with gravity correction
$j_E(x, y)$, W/mm^2	Energy flux density of a laser beam incident along the z-direction
$j_E^*(x, y, z)$, W/mm^2	Local energy flux density of the attenuated laser beam
n	Scattering exponent
$\vec{n}$	Outward normal of the workpiece surface
$p(x, y, z)$	Volume fraction of powder particles in the interaction zone
$p^*(x, y, z)$	Volume fraction of powder particles with gravity correction
q, q_L, $q_I(x, y, z)$, W/mm^3	Absorbed spatial power density distribution (L: laser, I: induction)
q_2, q_{2L}, $q_{2I}(x, y)$, W/mm^2	Absorbed power per unit area (L: laser, I: induction)
$\vec{q}_{ext}$, W/mm^2	Total external heat flux density through the workpiece surface
r_L, mm	Laser beam radius
$\vec{r}$, mm	Space vector
$\vec{r}_O$, mm	Position of the nozzle outlet
t, s	Time
$\vec{v} = v\,\vec{e}_x$, mm/s	Feed rate
v_0, m/s	Initial powder particle speed
w, mm	Bead width
$w(R)$, mm^{-1}	Distribution function of powder particle radii
x, mm	Coordinate along the feed direction
x_{max}, mm	Foremost position of the bead/melting zone
$x_{sol}(z)$, mm	Course of solidification front on the bead surface
y, mm	Coordinate on the substrate surface across the feed direction
z, mm	Coordinate perpendicular to the substrate surface
A, mm	Absorbed fraction of irradiated energy
E, N/mm^2	Young's modulus
F, mm^2	Area on the substrate surface covered by the powder stream
$G(z, t)$, mm^{-1}	Green's function of the one-dimensional heat flow equation
$G_R(x, y, z)$, mm^{-1}	Rosenthal's solution of heat flow equation for a moving point source
$\underline{I}$	Second rank unit tensor
J, g/s	Mass flow (powder rate)
L, mm	Distance between nozzle outlet and target point
Q_P, Ws/g	Latent heat of melting (powder material)
R, m, mm	Radius (of plate curvature, of particle)
T, °C	Temperature
T_0, C	Initial temperature
T_{lim}, C	Minimum required temperature for particles to be resorbed
T_M, T_{MS}, T_{MP}, C	Melting point temperature, of substrate, of the powder
$T_P(x, y, z; R)$, °C	Temperature of a particle with radius R at position (x, y, z)
T_U, C	Ambient temperature
$Z(x, y; \alpha_C)$, mm	Local bead height
α, W/(mm^2 K)	Heat transfer coefficient
$\alpha_C \equiv \gamma/(g\rho_0 b^2)$	Capillarity parameter
β	Geometry parameter
χ	Shear factor in the ellipsoid model
δ, mm	Penetration depth of the electromagnetic field
$-\delta z(\vec{r})$, mm	Local gravity induced correction of particle trajectory
$\underline{\varepsilon}$, ε_{xx}	Total strain tensor, strain component
$\underline{\varepsilon}^E$, ε_{xx}^E	Elastic strain tensor, component
$\underline{\varepsilon}^I$, ε_{xx}^I	Inelastic strain tensor, component
$\underline{\varepsilon}^P$, ε_{xx}^P	Plastic strain tensor, component
$\underline{\varepsilon}^T = \varepsilon_T\,\underline{I}$	Thermometallurgical strain tensor
γ, N/mm	Surface tension
η, mm	Thickness of the equivalent heat source layer
κ, mm^{-1}	Plate curvature
λ, W/(mm K)	Heat conductivity
μ	Relative magnetic permeability
μ_0, Vs/(A mm)	Permeability constant
ν	Poisson's ratio
ρ, V mm/A	Electrical resistivity
ρ_0, g/mm^3	Mass density
$\underline{\sigma}$, N/mm^2	Stress tensor
σ_{xx}, N/mm^2	Longitudinal stress component
σ_{yy}, N/mm^2	Transverse stress component
σ_Y, N/mm^2	Yield stress

τ, s	Characteristic time of cooling by convection	Δz, mm	Interval on the z-axis
ω, s^{-1}	Circular frequency	ΔQ_R, W	Amount of reflected power
Δt, Δt_i, s	Time interval of heating, inductive heating	ϑ	Scattering angle
		$\Theta(x)$	Heaviside's step function
$\Delta m/\Delta x$, g/mm	Powder mass deposited per unit length	Ω	Space angle
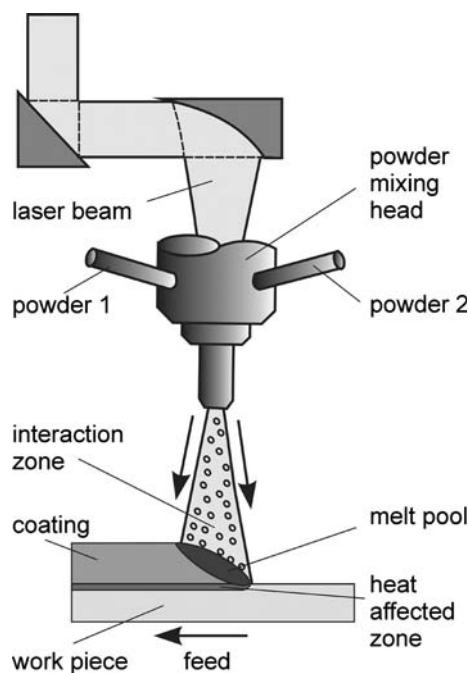
Fig. 1 Laser cladding

difference model of the temperature field in the process zone using some assumptions on the melt pool shape. In 1990, Li, Steen, and Hibberd (Ref 2) developed software that connects empirically found relations between process parameters and results of treatment in order to find suitable sets of process parameters for given tasks.

During the 1990s, a series of papers were published that treated the interaction of the powder particles with the laser beam (Ref 3-7). These theories have been refined more recently by considering the heat exchange between the flying powder particles and the carrier gas, the influence of the nozzle geometry, and the evaporation of strongly heated particles (Ref 8-13). Numerical calculations of temperature field and fluid flow in the melt pool have been performed first within the framework of two-dimensional models (Ref 14-19). In 1994, Picasso et al. (Ref 20) determined using three-dimensional analytical expressions of the temperature field those values of process parameters such as feed rate and powder rate that are required to obtain a prescribed bead size.

A series of closed models, that regard most of the interrelated processes in laser cladding such as preheating of the powder particles crossing the laser beam and the related beam attenuation, the powder resorption by the melt pool, and the evolution of temperature field and bead

geometry, were published during the last few years (Ref 21-31).

Based on the energy and mass balance, Kaplan and Groboth (Ref 21) developed a process model including powder heating, formation of coating beads, substrate dilution, and track overlapping. The powder mass flow rate and the geometrical properties of the beam and of the powder jet were used to optimize the powder catchment efficiency and the beam energy redistribution in the material.

Lepski et al. (Ref 22-25) developed a model of laser cladding with coaxial or off-axis powder supply that determines bead shape and temperature field in a self-consistent manner using a boundary element method. In order to save calculation time, they describe the bead shape by an analytical expression with free parameters to be fitted to the temperature field in an iterative procedure. The corresponding software tool compares the obtained results with the required bead shape and derives recommendations on how to correct the process parameters. In this way, a suitable set of process parameters is achieved after a few simulation runs.

A three-dimensional quasi-stationary finite element model (FEM) of laser cladding with coaxial powder injection was published by Pirch et al. (Ref 26). Temperature field and bead geometry are calculated numerically in a self-consistent manner. The obtained temperature gradients and cooling rates are used to get predictions of the solidification structure of the coating.

Toyserkani et al. (Ref 27) presented a three-dimensional transient finite element model of the bead formation. The bead is built-up by a series of layers, the width and height of which are determined by the molten area of the preceding layer and the resorbed powder mass. In that model, the influence of beam velocity, laser power, powder jet geometry, laser pulse shaping, and temperature-dependent material properties on the cladding results was considered, whereas the influence of surface tension and gravity force on the bead shape was neglected.

Ahlström et al. (Ref 28) modeled the laser cladding process on medium-carbon steel. In that work the main focus was to obtain the resulting microstructure. The phase transformations were integrated into a finite element model, and the temperature field was calculated by means of analytical solutions of the heat flow equation.

A fully numerical model based on a finite difference method was published by Han et al. (Ref 29-31). Powder preheating, heat transfer in the substrate and fluid flow in the melt pool, the role of latent heat, and phase transformations were simulated. Energy losses by reflection, convection, thermal radiation, and evaporation were

taken into account, and the evolution of the free melt pool surface was calculated by means of the level set method. The momentum transfer due to the impinging particles was found to be responsible for fluctuations of melt pool surface and fluid flow.

First calculations of the thermo-mechanical history of coatings deposited by laser cladding were published about 10 years ago. Those early papers (Ref 32-35) used one-dimensional and generalized plane strain finite element models for calculating the residual stress after the deposition of a liquid layer, for example, of stainless steel on a carbon steel. De Deus and Mazumder (Ref 36) calculated temperature field and thermal stress for a coating of a copper alloy on an aluminum substrate using a generalized plane strain finite element model with an elastic-perfectly plastic material behavior. This model has been extended to a three-dimensional one by de Deus in his dissertation (Ref 37). Nickel et al. (Ref 38, 39) investigated the influence of the track pattern and of the thickness of the coating on the thermal stress in shape deposition manufacturing using a three-dimensional finite element model. Thereby a single bead was assumed to be generated as a whole during a short time interval. The influence of the bead shape on the temperature field was not considered. The model was used to optimize track pattern and coating thickness with respect to distortion. Kahlen and Kar (Ref 40) investigated the relationship between melt pool geometry, solidification front, and residual stress. Dai and Shaw (Ref 41) calculated stresses in ceramic metal composites on artificial tooth. The influence of phase transformations on residual stresses had not been taken into account so far.

A three-dimensional simulation of the thermometallurgical and mechanical history of two beads generated one after the other was carried out recently by Ghosh and Choi (Ref 42, 43), who took into account phase transformations and transformation plasticity but, unfortunately, did not perform a self-consistent calculation of bead shapes and temperature field before. The high sensitivity of the results to the material properties, especially the phase transformation behavior, was emphasized by the authors.

Using FEM, Jendrzejewski et al. (Ref 44-46) calculated temperature distributions and residual stresses in Stellite SF6 coatings on steel X10Cr13 substrates with and without preweld heating in a furnace. From reading Ref 44, it is suspected that plastic deformation was not considered at all in calculating the mechanical response on thermal contraction. As a consequence, stresses of about 2 GPa and more were obtained for laser cladding without preheating. In our opinion this neglect is not justified in any way for Stellite coatings. Without preheating, a model with a purely elastic material behavior would yield stresses far beyond the tensile strength even for material couples such as Stellite 21 on steel Ck45 where cracks usually are not observed.

Residual stress and distortion of a cantilever beam made from stainless steel with a nickel-base metal-matrix composite coating containing WC inclusions were calcu-

lated and discussed in detail by Plati et al. (Ref 47) using a model with elastic-perfectly plastic material behavior.

Despite doubtlessly great progress during the last few years, there still remains a lack of simulation tools that enable quick prediction of those process parameter values that are required for certain desired results of cladding. Moreover, information is urgently needed, on how to optimize track pattern and process parameters in order to reduce residual stresses and thermal distortion and to avoid cracks (Ref 48).

This article investigates possibilities of reducing residual stress and the danger of cracking by preweld or postweld heating using electromagnetic inductors integrated directly into the cladding process. Based on previous work on the simulation of laser cladding (Ref 22-25), a three-dimensional transient finite element model is developed that is able to improve our knowledge of the influence of process parameters and material properties on the evolution of stress and inelastic strain in laser cladding.

3. Visualization of Stress and Strain Evolution Using an Analytical One-Dimensional Model

Thermal stress and distortion are determined in a rather complicated way by thermal expansion and contraction proceeding simultaneously or one after the other in adjacent parts of the considered body, by thermally induced phase transformations, and by accompanying phenomena such as plastic flow and transformation plasticity, which also depend on temperature, temperature rate, and the changing distribution of phase volume fractions. Therefore, it is very difficult to understand in detail the mechanisms of the strain and stress evolution in laser cladding and their dependence on the process parameters. However, the most important phenomena can be visualized and understood in principle using a quite simple analytical one-dimensional model.

Let us consider a wide plate of thickness h lying in the x-y plane. During the short time interval $\Delta t = t_1 - t_0$, one plate surface is heated up to the melting point, and a molten layer of the coating material of thickness d is deposited on it. Thereafter, the heat is conducted into the substrate and the coating solidifies and starts shrinking due to thermal contraction, whereas the substrate first expands and later contracts according to the local thermal cycle. This thermal strain can be modified by the formation of phases with different densities. The resulting inhomogeneous thermometallurgical strain $\underline{\varepsilon}^{T}$ causes thermal stress. Plastic flow occurs if the stress exceeds a flow criterion that depends on temperature and phase fractions and on previous plastic strain increments.

3.1 Temperature Field

The heat source acting on the plate surface within the time interval $t_0 \leq t \leq t_1$,

$$q(z) = q_2 \lim_{\varepsilon \to 0} [\delta(z - \varepsilon) + \delta(z + \varepsilon)] \, \Theta(t - t_0) \, \Theta(t_1 - t),$$

(Eq 1)

generates the temperature field, which is calculated by means of the time-dependent Green's function $G(z, t)$ of the one-dimensional heat flow equation using mirror sources to fulfill zero heat flux boundary conditions at the surfaces ($\Theta(x)$: Heaviside's step function):

$$G(z,t) = \frac{\Theta(t)}{\sqrt{4\pi at}} \sum_{j=-\infty}^{\infty} \exp\left(-\frac{(z-2hj)^2}{4at}\right)$$

$$T - T_0 = \frac{a}{\lambda} \int_{-\infty}^{\infty} dt' \int_{-\infty}^{\infty} dz' \, q(z') \, G(z - z', t - t')$$

$$= \frac{2q_2}{\lambda} \sum_{j=-\infty}^{\infty} \left[\Theta(t - t_0) \sqrt{4a(t-t_0)} \, ierfc\left(\frac{z - 2hj}{\sqrt{4a(t-t_0)}}\right) \right.$$

$$\left. - \Theta(t - t_1) \sqrt{4a(t-t_1)} \, ierfc\left(\frac{z - 2hj}{\sqrt{4a(t-t_1)}}\right) \right]$$

(Eq 2)

Thereby a and λ are the uniform values of the heat diffusivity and heat conductivity of the material, respectively.

For long times and/or thin plates with $t - t_1 \gg h^2/a$ the series in Eq 2 converges rather slowly since a lot of mirror sources must be considered. In that case, it is better to expand the periodic function $G(z, t)$ into a Fourier series that converges very rapidly at long times:

$$G(z,t) = \frac{1}{h}\left\{ \frac{1}{2} + \sum_{n=1}^{\infty} \exp\left[-\left(\frac{\pi n}{h}\right)^2 at \right] \cos\left(\frac{\pi n z}{h}\right) \right\},$$

$$T - T_0 = \frac{q_2 h}{\lambda}\left\{ \frac{a(t_1 - t_0)}{h^2} + 2\sum_{n=1}^{\infty} \frac{\cos\frac{\pi n z}{h}}{\pi n} \left[\exp\left[-\left(\frac{\pi n}{h}\right)^2 a\left(t - t_1\right) \right] \right.\right.$$

$$\left.\left. - \exp\left[-\left(\frac{\pi n}{h}\right)^2 a(t - t_0) \right] \right] \right\}.$$

(Eq 3)

In addition, convection cooling by the surrounding medium with a heat transfer coefficient α is taken into account. If $\alpha h \ll \lambda$, this cooling proceeds much more slowly than the heat equilibration within the plate and hence becomes important at long times only. Then the diffusion term in the heat diffusion equation can be neglected, and we obtain an exponential decay of the equalized, almost homogeneous plate temperature (initially T_1) during time:

$$\rho_0 c h \frac{dT}{dt} \approx -2\alpha \, (T - T_U),$$

$$T - T_U \approx (T_1 - T_U) \exp\left(-\frac{t}{\tau}\right), \quad \tau \equiv \frac{\rho_0 c h}{2\alpha}.$$

(Eq 4)

3.2 Mechanical Model

Within the framework of the linear theory of elasticity, stress depends linearly on the elastic strain $\underline{\underline{\varepsilon}}^E$, that is the difference of the total strain $\underline{\underline{\varepsilon}}$ and the inelastic strain $\underline{\underline{\varepsilon}}^I$,

which consists of the thermometallurgical strain $\underline{\underline{\varepsilon}}^T$ and the cumulative plastic strain $\underline{\underline{\varepsilon}}^P$ including transformation plasticity:

$$\underline{\underline{\sigma}} = \frac{E}{1 + v}\left[\underline{\underline{\varepsilon}}^E + \frac{v}{1 - 2v} \underline{\underline{I}} \, \mathrm{Tr} \, \underline{\underline{\varepsilon}}^E \right], \, \underline{\underline{\varepsilon}}^E = \underline{\underline{\varepsilon}} - \underline{\underline{\varepsilon}}^I,$$

$$\underline{\underline{\varepsilon}}^I \equiv \underline{\underline{\varepsilon}}^T + \underline{\underline{\varepsilon}}^P, \underline{\underline{\varepsilon}}^T = \varepsilon_T \underline{\underline{I}}, \mathrm{Tr} \, \underline{\underline{\varepsilon}}^P = 0.$$

(Eq 5)

Here E and v are Young's modulus and Poisson's ratio, respectively. The symbols underlined twice represent second-rank tensor quantities, $\underline{\underline{I}}$ being the second-rank unit tensor. In isotropic bodies thermometallurgical strain causes isotropic expansion or contraction, whereas plastic flow does not change the volume.

As it takes place sufficiently far from the lateral plate boundaries the deformation of the plate is independent of x and y. From the compatibility conditions for the total strain tensor, a linear dependence of its components $\varepsilon_{xx} = \varepsilon_{yy}$ on z is derived:

$$\frac{\vec{\partial}}{\partial \vec{r}} \times \underline{\underline{\varepsilon}} \times \frac{\vec{\partial}}{\partial \vec{r}} = 0 \Rightarrow \frac{\partial^2 \varepsilon_{xx}}{\partial z^2} = \frac{\partial^2 \varepsilon_{yy}}{\partial z^2} = 0$$

$$\Rightarrow \varepsilon_{xx} = \varepsilon_{yy} = \overline{\varepsilon_{xx}} + \kappa z.$$

(Eq 6)

If the origin of the z-axis is assumed in the middle of the plate, then ε_{xx} describes an average expansion or contraction $\overline{\varepsilon_{xx}}$ and a homogeneous bending with the curvature κ to be determined from the equilibrium conditions

$$\frac{\vec{\partial}}{\partial \vec{r}} \cdot \underline{\underline{\sigma}} = 0 \quad \Rightarrow \quad \frac{\partial \sigma_{zz}}{\partial z} = 0 \quad \Rightarrow \quad \sigma_{zz} = 0,$$

$$\int_{-\frac{h+d}{2}}^{\frac{h+d}{2}} dz \, \sigma_{xx}(z,t) = 0, \quad \int_{-\frac{h+d}{2}}^{\frac{h+d}{2}} dz \, z \, \sigma_{xx}(z,t) = 0.$$

(Eq 7)

If the modulus of the stress, $|\sigma_{xx}|$, achieves the yield stress, σ_Y, the onset of plastic flow prevents an increase of stress beyond the yield stress. The plastic strain increments then follow from Eq 5 and 7 taking into account the influence of strain hardening on the yield stress:

$$|\sigma_{xx}| = \sigma_Y,$$

$$\delta \varepsilon_{xx}^P(z,t) = \varepsilon_{xx}(z,t) - \varepsilon_T(z,t) - \varepsilon_{xx}^P(z, t - \delta t)$$

$$- \frac{1 - v}{E(z,t)} \sigma_Y\left[z, t, \sum_i |\delta \varepsilon_{xx}^P(z, t_i < t)| \right] \mathrm{sign}(\sigma_{xx}).$$

(Eq 8)

The dependence of Young's modulus and yield strength on temperature and phase volume fractions, the phase transformation kinetics, and isotropic strain hardening have been taken into account. Material data of Stellite 21 and steel Ck45 were used.

3.3 Evolution of Stress and Inelastic Strain

As an example, Fig. 2(a) and (b) show the calculated thermal as well as stress and plastic strain histories in a plane below the substrate-coating interface. Obviously, periods with elastic ($|\sigma_{xx}| < \sigma_Y$) and elastic-plastic behavior alternate in time.

The final cumulated plastic strain in the substrate may result from compressive and tensile increments because of periods with plastic flow in thermal expansion and contraction, respectively (Fig. 2a, b). Within the coating the plastic strain is purely tensile, and in most cases it becomes much higher than in the substrate (Fig. 2d). Phase transformations may yield additional contributions to plastic strain and stress due to density changes and transformation plasticity (Ref 49-53).

Cracks usually arise if the stress reaches the ultimate tensile strength or the sum of the absolute plastic strain increments exceeds the fracture strain. The latter, however, strongly depends on temperature. Hence plastic strain increments have to be properly weighted by a temperature-dependent factor if their relevance to cracking is to be assessed.

Figures 2(c) and (d) show the resulting stress and strain distributions within the plate after the latter has reached the ambient temperature. In the absence of any irreversible phase transformation (e. g., formation of martensite), the thermometallurgical strain then becomes zero in the substrate but has a large negative value due to thermal contraction in the coating (region 1 in Fig. 2c) which is compensated for by large positive plastic strain and positive elastic strain causing tensile stress.

In the substrate near the coating, thermal expansion during heating temporarily leads to compressive stress that is partially reduced by plastic flow causing negative plastic strain. The consequence is tensile residual stress in regions 3 and 4 of Fig. 2(c). In region 3, additional positive

plastic strain increments arise during cooling (Fig. 2b) that finally reduce the residual tensile stress. Enhanced plastic flow occurs during cooling within the γ phase in that part of the substrate (region 2 of Fig. 2c) that was transformed into austenite and gives rise to compressive stress in that range.

The conditions that the total force and moment acting on each volume element must be zero determine the resulting total strain ε_{xx}. According to Eq 5, residual stress follows from:

$$\sigma_{xx} = \frac{E}{1-v}\left(\varepsilon_{xx} - \varepsilon_{xx}^{I}\right), \varepsilon_{xx}^{I} \equiv \varepsilon_{xx}^{P} + \varepsilon_{T}. \qquad \text{(Eq 9)}$$

If the actual distribution of inelastic strain, $\varepsilon_{xx}^{I}(z)$, that is, the sum of thermometallurgical strain and cumulated plastic strain, is known over the whole plate thickness, the corresponding stress $\sigma_{xx}(z)$ and the coefficients of the total strain ε_{xx} (see Eq 6) can be calculated from Eq 7 and 9. Assuming for the moment the Young's modulus E to be independent of z and $d \ll h$ these coefficients are approximately given by

$$\overline{\varepsilon_{xx}} \approx \frac{1}{h}\int\limits_{-\frac{h+d}{2}}^{\frac{h+d}{2}} dz\,\varepsilon_{xx}^{I}(z), \kappa \approx \frac{12}{h^3}\int\limits_{-\frac{h+d}{2}}^{\frac{h+d}{2}} dz\, z\,\varepsilon_{xx}^{I}(z). \qquad \text{(Eq 10)}$$

The influence of the total strain ε_{xx} on σ_{xx} shown by Eq 9 explains the occurrence of residual stress even in region (5) of Fig. 2(c), where both thermometallurgical and plastic strain are zero at the end of the cladding process.
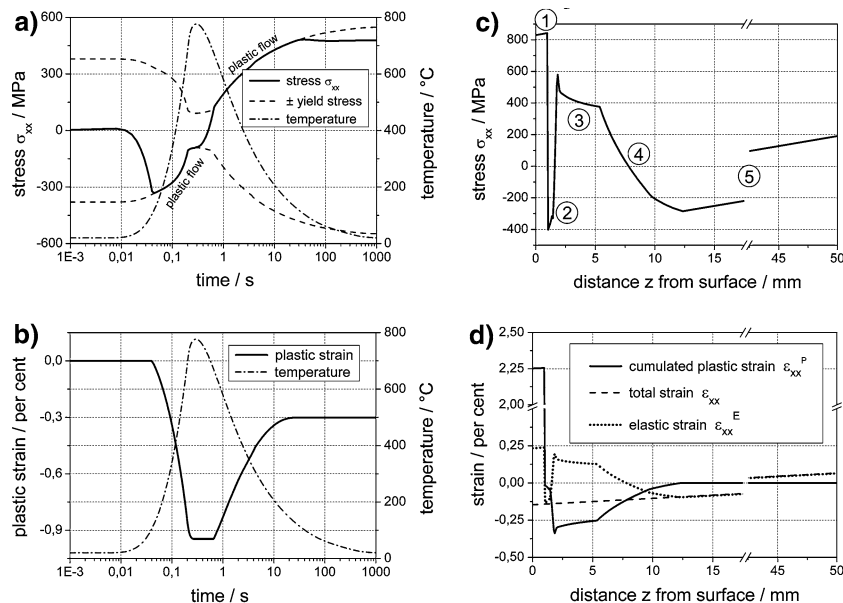

Fig. 2 History and final state of strain and stress for a coated plate, calculated with the one-dimensional model (parameters: plate thickness $h = 50$ mm, coating thickness $d = 1$ mm, heating time $\Delta t = 0.2$ s, maximum temperature = 1500 °C, absorbed power density = 17.6 W/mm², materials: stellite 21 coating on steel Ck45). (a) Thermal and stress history at a depth of 1 mm below the substrate/coating interface. (b) Temperature and plastic strain vs. time at 1 mm below the substrate/coating interface. (c) Residual stress σ_{xx} versus z showing regions 1 to 5 with different mechanisms of stress evolution (see text), (d) final distribution of total strain, plastic strain, and elastic strain in the plate

3.4 Influence of Selected Parameters on Residual Stress and Distortion

The simple model shows what happens in principle if some parameters are changed. If, for example, heating time is increased, heat may penetrate deeper into the plate. With increasing heating time, that part of the substrate becomes larger where tensile residual stresses arise after cooling as a consequence of plastic compression during heating. As a result, the total strain $\overline{\varepsilon_{xx}}$ becomes more negative, that is, the plate contracts more strongly as a whole, with the consequence that the tensile stress in the coating is reduced (see Fig. 3a).

Preheating is reported to be an appropriate tool to prevent cracking and delamination of the coating (Ref 54-57). It enables heat to equalize (almost completely) in the body at a rather high temperature level. Therefore, stresses related to temperature gradients are less pronounced and may be released by less plastic flow proceeding at comparatively high temperatures. This can help to prevent cracks since many materials tolerate large strain much better at higher temperatures. Thereafter, the whole plate cools down rather slowly to the ambient temperature. However, different expansion coefficients of the two welded materials may enhance the stress in this stage again. Then residual stress may become almost independent of the initial temperature (Fig. 3b).

This statement is also confirmed by Fig. 3(c) and (d), which give the evolution of temperature and stress in the coating for initial temperatures of 20 and 600 °C, respectively. Figure 3(d) shows that this stress increases further even after an almost homogeneous temperature level in the entire plate has been reached, since the Stellite coating contracts more rapidly than the steel substrate during further cooling.
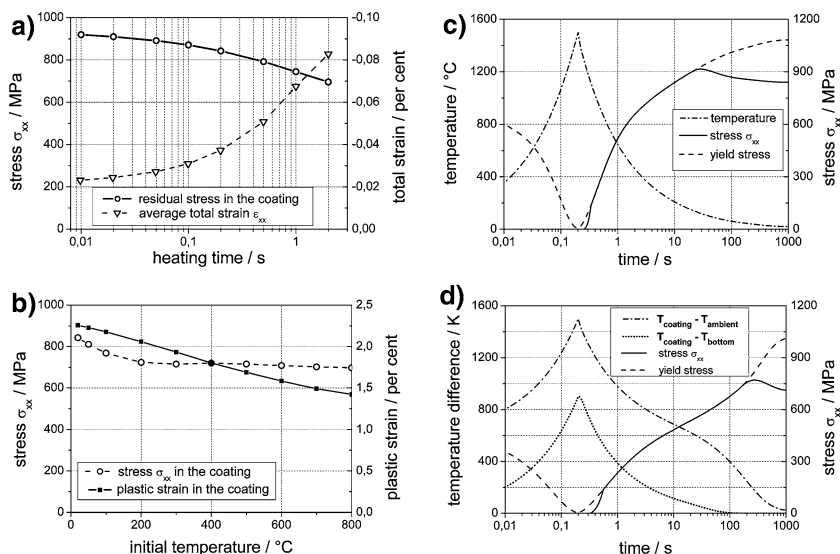
Last but not least, preheating is even able to reduce distortion as shown in Fig. 4. Following Eq 10, the coefficients of the total strain (Eq 6) are determined by the zeroth and first-order moments of the residual inelastic strain (Fig. 4b), which become smaller with increasing preheating temperature (Fig. 4a). This may be understood as follows: Without preheating, thermal contraction of the coating and plastic flow during thermal expansion of the substrate cause negative residual inelastic strain in both the coating and the adjacent part of the substrate, finally leading to contraction in that range. However, with increasing preheating temperature that part of the substrate is enlarged that is temporarily transformed into austenite. Strong positive plastic strain may arise there during cooling (regions 2 in Fig. 2c and 4b). Hence, for low initial temperatures, the plate contracts as a whole and is strongly bent, whereas it is only weakly distorted after appropriate preheating.

Summarizing, it may be stated that the described one-dimensional model is able to qualitatively explain the influence of plastic flow and of material properties, as for example, phase transformations, differences of heat expansion coefficients, Young's moduli or yield stresses of coating and substrate, as well as the influence of various process parameters on stress and strain in laser cladding without complex numerical calculations. The use of analytical solutions facilitates the understanding of the observed effects. On the other hand, the model disregards the local character of the laser treatment, which means it neglects the lateral heat flow and the different thermal and mechanical histories of adjacent volumes. Therefore, the obtained cooling rates are too small, and stress and strain are overestimated. More accurate results have to be obtained by means of numerical methods, for example, the finite element method.
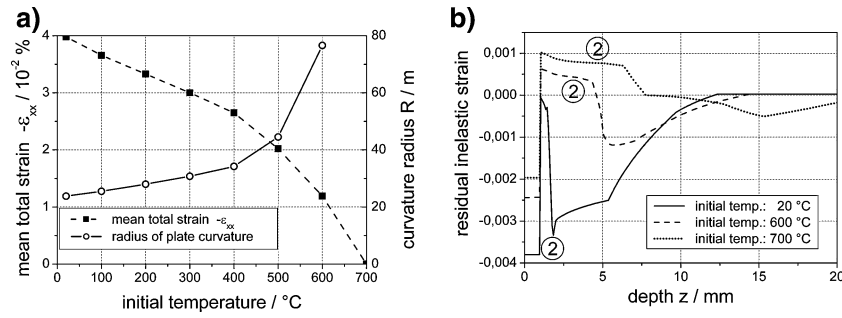

Fig. 3 Dependence of residual stress and strain in the coating on heating time and preheating temperature. Parameters not mentioned here are chosen as in Fig. 2. (a) Maximum residual stress in the coating and average total strain $\overline{\varepsilon_{xx}}$ vs. heating time. (b) Stress and plastic strain in the coating as functions of the initial temperature: preheating leads to a noticeable reduction of plastic strain but can lessen the residual stress only slightly for this couple of materials. (c) Temperature, T; stress, σ_{xx}; and yield stress, σ_Y; in the coating vs. time if plate heating started at 20 °C. (d) as in (c) but for an initial temperature of 600 °C. The actual maximum temperature difference in the plate is shown too. The stress in the coating is still growing after heat has (almost) completely equalized, since the Stellite coating contracts more rapidly during cooling than the steel substrate

Fig. 4 Influence of initial temperature on distortion: (a) average total strain and the plate's curvature radius, $R = 1/\kappa$, versus initial temperature (b) distribution of the residual inelastic strain (sum of thermometallurgical and plastic strain) for various initial temperatures. As in Fig. 2c, the symbol (2) marks regions where, for the given initial temperature, austenite had been formed during the thermal cycle

4. Modeling of Bead Formation and Stress Evolution in Laser Cladding

4.1 Process Modeling

For more accurate three-dimensional calculations of the residual stresses in laser cladding by means of a commercial finite element code, one must know the shape of the built-up welded bead and that equivalent heat source that would yield the laser-induced temperature field by pure heat conduction.

To this end the whole cladding process has to be simulated taking into account the interaction between laser beam and powder jet, the powder resorption by the melt pool, and the formation of temperature field and bead shape.

4.1.1 Particle Density Distribution and Mass Flow in the Powder Stream. Omitting for the moment the effect of gravity on the powder particles flying from the nozzle to the workpiece, we describe the mass flow density in the powder stream as a function of the scattering angle ϑ of the particles around the average flight direction $\overline{OZ}$ (see Fig. 5a) and of the distance from the nozzle:

$$\vec{j}(\vec{r}) = J \frac{n+1}{2\pi} \cos^n \vartheta \frac{\vec{r} - \vec{r}_O}{|\vec{r} - \vec{r}_O|^3}, \cos \vartheta = \frac{(\vec{r} - \vec{r}_O) \cdot (\vec{r}_Z - \vec{r}_O)}{L|\vec{r}_O - \vec{r}|}.$$

(Eq 11)

Here J is the total mass flow emitted by the nozzle, $\vec{r}_O$ is the position of the nozzle outlet, $\vec{r}_Z$ is that of the central target point with coordinates $(0, 0, 0)$, L is the distance between these two points and n is a scattering exponent to be determined from the observed area F, which is covered by the powder jet at the substrate surface, $z = 0$ (see also Fig. 5a):

$$-\int \int_F dx dy \, \vec{e}_z \cdot \vec{j}(x, y, 0) = 0.86 \, J \Rightarrow n$$

(Eq 12)

Thereby the z-axis points into the direction of the outward substrate surface normal. The mass flow density $\vec{j}(\vec{r})$ is related to the local volume fraction $p(\vec{r})$ of powder particles (ρ_0: density of powder material, v_0: average initial speed of particles at the nozzle):

$$\vec{j}(\vec{r}) = \rho_0 v_0 p(\vec{r}) \frac{\vec{r} - \vec{r}_O}{|\vec{r} - \vec{r}_O|},$$

$$p(\vec{r}) = \frac{J}{\rho_0 v_0} \frac{n+1}{2\pi} \frac{\left[\frac{L^2 - zz_O - xx_O}{L\sqrt{y^2 + (x-x_O)^2 + (z-z_O)^2}}\right]^n}{y^2 + (x-x_O)^2 + (z-z_O)^2}$$

(Eq 13)

For common particle velocities of more than 2 m/s it holds that $gL/v_0^2 \ll 1$ and the effect of gravity can be neglected. This effect, however, may strongly influence the trajectories of the particles if their initial speed v_0 is reduced to melt the powder before it reaches the workpiece surface.

With gravity, the particles will reach positions with coordinates z that are less than those expected without gravity by an amount $\delta z(\vec{r}) = g \, t^2(\vec{r}) / 2$, where $t(\vec{r})$ is the flight time from the nozzle outlet to the given point $\vec{r}$. With gravity, therefore, we will find those particles at positions z and $z + \Delta z$, which without gravity were at positions $z + \delta z \,(x, y, z)$ and $z + \Delta z + \delta z \,(x, y, z + \Delta z)$, respectively. Therfore, particles reaching points within a small interval of length Δz around z with gravity, would be found within an interval of length $\Delta z \,[1 + \partial \delta z / \partial z]$ without gravity. Thus the modified powder volume fraction $p^*(\vec{r})$ and mass flow density $\vec{j}^*(\vec{r})$ are derived from Eq 13:

$$p^*(\vec{r}) = p(\vec{r}^*) \left[1 + \frac{\partial \delta z(\vec{r})}{\partial z}\right],$$

$$\vec{j}^*(\vec{r}) = \rho_0 \, p^*(\vec{r}) \left[v_0 \frac{\vec{r}^* - \vec{r}_O}{|\vec{r}^* - \vec{r}_O|} + \vec{g} \sqrt{\frac{2\delta z(\vec{r})}{g}}\right],$$

$$\delta z(\vec{r}) = \frac{g}{2v_0^2} (\vec{r}^* - \vec{r}_O)^2$$

$$= \frac{(z - z_O) [1 - w(x, y, z)] + \frac{g}{v_0^2} \left[(x - x_O)^2 + y^2\right]}{1 + w(x, y, z)},$$

$$1 + \frac{\partial \delta z(\vec{r})}{\partial z} = \frac{1}{w(x, y, z)},$$

$$w(x, y, z) \equiv \sqrt{1 - 2\frac{g}{v_0^2}(z - z_O) - \left(\frac{g}{v_0^2}\right)^2 \left[(x - x_O)^2 + y^2\right]},$$

$$\vec{r}^* \equiv \vec{r} + \delta z(\vec{r}) \, \vec{e}_z, \vec{g} = -g \, \vec{e}_z.$$

(Eq 14)

Therefore the solution of the quadratic equation for δz had to be chosen that vanishes at the position $\vec{r}_O = (x_O, 0, z_O)$ of the nozzle outlet. Inserting this solution into the expressions for the powder volume fraction $p^*(\vec{r})$ and the powder mass flow $\vec{j}^*(\vec{r})$ in the interaction zone yields the following final formulae to be used in the subsequent calculations:

$$p^*(x,y,z) = \frac{J}{\rho_0 v_0} \frac{n+1}{2\pi} \frac{\left[\frac{L^2 - z_O(z+\delta z(\vec{r})) - x_O x}{L\sqrt{y^2 + (x-x_O)^2 + (z+\delta z(\vec{r}) - z_O)^2}}\right]^n}{\left[y^2 + (x-x_O)^2 + (z+\delta z(\vec{r}) - z_O)^2\right]\sqrt{1 - 2\frac{g}{v_0^2}(z-z_O) - \left(\frac{g}{v_0^2}\right)^2\left[(x-x_O)^2 + y^2\right]}},$$
(Eq 15)

$$\vec{j}^*(x,y,z) = \rho_0 v_0 p^*(x,y,z) \frac{(x-x_O)\vec{e}_x + y\vec{e}_y + (z+\delta z(\vec{r}) - z_O)\vec{e}_z + \frac{\vec{g}}{v_0^2}\left[(z+\delta z(\vec{r}) - z_O)^2 + (x-x_O)^2 + y^2\right]}{\sqrt{(z+\delta z(\vec{r}) - z_O)^2 + (x-x_O)^2 + y^2}},$$

For a coaxial nozzle the corresponding quantities are obtained by superposition of the contributions of single-point sources of powder distributed uniformly over an annular nozzle.

4.1.2 Interaction between Laser Beam and Powder Stream. The laser light is partly absorbed and reflected by the flying particles. Thus the particles are preheated and the energy flux density $j_E(x,y)$ of a laser beam incident along the z-direction is attenuated yielding a modified energy flux distribution $j_E^*(x,y,z)$ according to

$$dj_E^*(x,y,z) = \beta\, j_E^*(x,y,z)\, p^*(x,y,z)\, \frac{dz}{R},$$
$$j_E^*(x,y,z) = j_E(x,y)\, \exp\left[-\beta \int_z^\infty \frac{dz'}{R} p^*(x,y,z')\right],$$
(Eq 16)

where R is the particle radius (or another characteristic length of the particle) and β a geometric factor ($\beta = 0.75$ for spherical particles). An averaging procedure over R may be required if the particle size scatters over a wide range. Figure 5(b) shows an example of such an attenuated laser beam.

A particle crossing the laser beam is preheated up to a temperature that depends on its individual trajectory, mass, and speed. Heating of particles is calculated using an energy balance regarding absorption of the incident energy of the laser beam and of the radiation reflected at the workpiece surface on the one hand and energy losses due to thermal radiation and convection on the other hand. Light reflected at particles is considered as lost.

For the reflection of the laser light at the workpiece surface a diffuse scattering law proportional to $\cos\vartheta$ is assumed, ϑ being the angular deviation of the scattering direction from the substrate surface normal. Hence, the power ΔQ_R that is scattered from all the points $\vec{r}'$ of the

substrate surface plane ($z' = 0$) into the corresponding space angle elements $\Delta\Omega(\vec{r} - \vec{r}')$ covered by a small spherical particle of radius R at position $\vec{r} = (x, y, z)$ is given by

$$\Delta\Omega(\vec{r} - \vec{r}') = 2\pi\left[1 - \sqrt{1 - \left(\frac{R^2}{|\vec{r} - \vec{r}'|^2}\right)}\right], z > R,$$

$$\Delta Q_R(x,y,z) \approx (1-A)\left\{ \iint\limits_{\text{workpiece}} \frac{dx'dy'}{\pi} j_E^*(x',y',0)\right.$$
$$\times \frac{z\,\Delta\Omega(x-x',\, y-y',z)}{|\vec{r} - \vec{r}'|}$$
$$\left.\times - R^2 j_E^*(x,y,0)\Delta\Omega(0,0,z)\right\}.$$
(Eq 17)

The second term in Eq 17 takes account of the shadow of the considered particle.

Furthermore, evaporation and convection cooling were taken into account using a model of Liu and Lin (Ref 12, 13). To this end a system of two nonlinear ordinary differential equations for the specific enthalpy and radius of the particle has to be solved for each trajectory and particle size using a fourth-order Runge-Kutta procedure with step size control. As an example, Fig. 5(c) shows the calculated rise of particle temperature and the decrease of particle size for heating up to temperatures beyond the evaporation threshold. In Fig. 5(d), the radial distributions of those particles in coaxial laser cladding are represented, the final temperatures of which exceed the corresponding values on the temperature axis. Because of the latent heat of fusion, a discontinuity appears in that representation at the melting point.

4.1.3 Self-Consistent Simulation of Temperature Field, Powder Catchment, and Bead Shape. After the required energy and mass flow density distributions acting on the workpiece surface as well as the temperatures of the
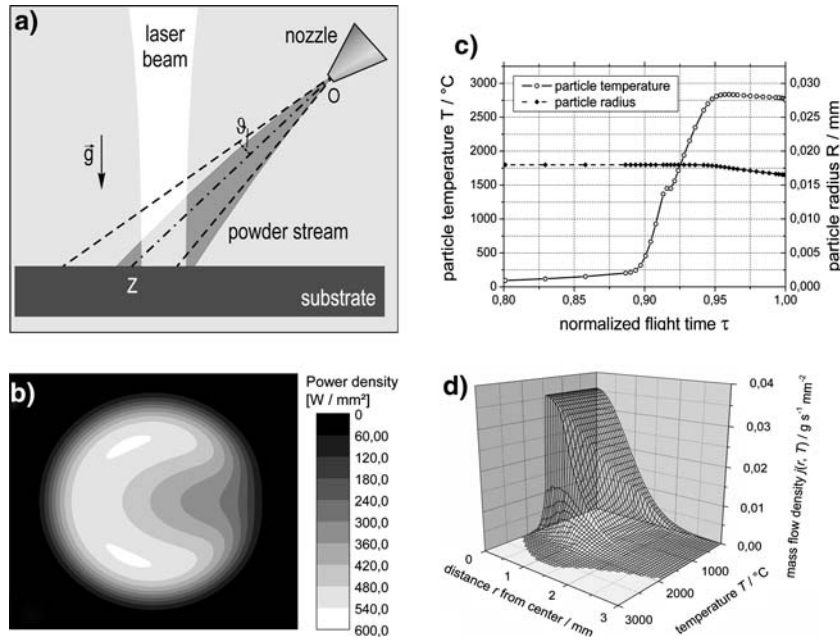
Fig. 5 Particle preheating and beam attenuation owing to the interaction of particle stream and laser beam (a) Geometrical scheme of laser cladding with off-axis powder supply suggesting the influence of gravity. Intensity distribution of a (rather strongly) attenuated laser beam (off-axis powder supply). Example of the evolution of particle temperature and radius during laser heating up to evaporation temperature. Radial powder mass flow density distributions $j(r,T)$ of those particles the final temperatures of which exceed the corresponding axis values T (coaxial powder supply)

impinging particles were obtained, the bead generation by powder injection into the laser-induced melt pool has to be simulated.

Powder particles may be caught by the melt pool if their temperatures are high enough that the particles are melted within the pool (otherwise they are driven to the melt pool edge and deposited there); the solid substrate if they already have been melted and the substrate temperature exceeds the melting point temperature T_{MP} of the powder material. The latter case, however, yields only something like a soldering connection between substrate and coating.

Hence, particles are resorbed by that part of the workpiece surface only, the temperature of which exceeds an effective melting temperature T_M given by:

$$
\begin{aligned}
T_M &= T_{MS} - (T_{MS} - T_{MP})\, \Theta(T_{MS} - T_{MP}) \\
&\quad \times [u\,\Theta(u) - (u-1)\,\Theta(u-1)], \\
u &\equiv \frac{h_P - c_P(T_{MP} - T_U)}{Q_P},
\end{aligned}
\tag{Eq 18}
$$

where T_{MS} and T_{MP} are the melting point temperatures of the substrate and the powder. Q_P, h_P, and c_P are the latent heat of fusion, the specific enthalpy, and the specific heat of the arriving particles.

Thus the bead width w is determined by the temperature field, whereas the bead cross-section shape $Z(y)$ follows from the conditions that the cross-sectional area is given by the amount of powder deposited per unit length, $\Delta m/\Delta x$, and the melt pool energy consisting of the surface energy and the potential energy in the gravity field becomes minimum:

$$
\delta \int_0^{w/2} dy \left[\sqrt{1 + \left(\frac{\partial Z}{\partial y}\right)^2}\, \gamma + \int_0^{Z(y)} dz'\, (\rho_0\, g\, z' + \phi) \right] = 0,
$$

$$
2 \int_{0_1}^{w/2} dy\, Z(y) = \frac{1}{\rho_0} \frac{\Delta m}{\Delta x}.
$$

(Eq 19)

The constant ϕ in this equation is a Lagrangian multiplicator.

The influence of the gravity term in Eq 19, obviously, depends on the capillarity parameter, $\alpha_C \equiv \gamma/(g\rho_0 b^2)$, with the surface tension γ, the gravity acceleration g, the density ρ_0, and a characteristical length of the bead (height or half width), b. As long as it holds $\alpha_C \gg 1$, that means, the bead width does not exceed a value of about 5 to 10 mm in the case of Stellite or similar coatings, surface tension is the predominant force that determines the melt pool shape. Then the upper borderline of the bead cross section will be almost circular.

In our model the shape of the bead and of the melt pool surface moving with the feed rate v along the x-axis is described by an analytical function $f(x - vt, y, z; \alpha_C) = 0$ with free parameters that have to be determined such as to fulfil the conditions just described.

To minimize the surface energy, we generate the surface of melt pool and bead from a sheared ellipsoid passing over to an elliptical cylinder at the solidification front $x_{sol}(z) = \chi(h - z)$:

$$f(x,y,z,\alpha_C) \equiv \Theta[x - \chi(h-z)] \left(\frac{x - \chi(h-z)}{aa}\right)^2$$

$$+ \left(\frac{y}{bb}\right)^2 + \left(\frac{z+cc-h}{cc}\right)^2 - 1 = 0.$$

$$\text{(Eq 20)}$$

This function contains initially unknown parameters as the half axes aa, bb, cc, the bead height h, and the shear parameter χ. The parameters aa and χ follow from the coordinates of three characteristic points on the boundary of the melted area, that is the front point of the bead at position $(x_{max}, 0, 0)$, the point of maximum melt pool width [position: $(x_{sol}(0), \pm w/2, 0)$], and the endpoint of the molten surface in the symmetry plane of the bead [position: $(x_{sol}(h), 0, h)$]:

$$x_{max} = \chi h + aa \sqrt{1 - (1 - h/cc)^2},$$

$$x_{sol}(z = 0) = \chi h, \quad x_{sol}(z = h) = 0.$$

$$\text{(Eq 21)}$$

These coordinates have to be derived from the shape of the melting point isotherm $(T = T_M)$ on the workpiece surface, whereas bb, cc, and h are determined by inserting the expression in Eq 20 with $x = 0$ into the variational condition (Eq 19) using the known actual values of the bead width w and of the mass deposited per unit length, $\Delta m/\Delta x$.

The function (Eq 20), however, still implies discontinuities of the surface normal at the melt pool boundary. The related discontinuities of the absorbed power per unit area may cause unrealistic minima of the calculated temperature distribution on the ellipsoid surface that may reach even values below the melting point. Therefore, the function (Eq 20) has to be modified to get a smooth transition from the substrate surface plane, $z = 0$, to the melt pool surface. To this end the constant half axis aa is transformed into a z-dependent function $aa(z)$ such that the intersection line between the melt pool surface and the symmetry plane $(y = 0)$ is described by a fourth-order polynomial of x with zero slopes at the front and backside boundaries of the melted range, $x = x_{max}$ and $x = x_{sol}(h)$, respectively:

$$\frac{z}{h} = P\left(\frac{x - x_{sol}(z)}{x_{max} - x_{sol}(0)}\right), \quad P(\xi) \equiv 3\xi^4 - 4\xi^3 + 1,$$

$$aa(z) = \frac{x_{max} - x_{sol}(0)}{\sqrt{1 - \left(\frac{z+cc-h}{cc}\right)^2}} P^{-1}\left(\frac{z}{h}\right),$$

$$P^{-1}(\zeta) = \left[2 + \sqrt{u(\zeta)} - \sqrt{12 - u(\zeta) + \frac{16}{\sqrt{u(\zeta)}}}\right] \Big/ 6,$$

$$u(\zeta) \equiv 4 + 6 \sqrt[3]{1 - \zeta} \left[\sqrt[3]{1 - \sqrt{\zeta}} + \sqrt[3]{1 + \sqrt{\zeta}}\right].$$

$$\text{(Eq 22)}$$

The resulting shape of melt pool and bead is shown in Fig. 6.

The temperature field in the process zone, which mainly determines the bead shape, is calculated by means
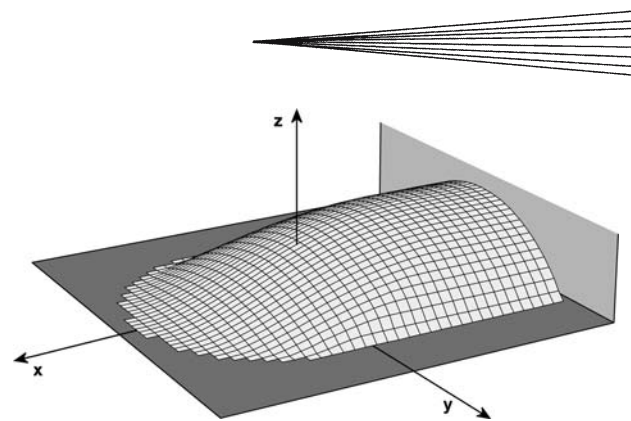

Fig. 6 Exemplary representation of the analytical function $f(x - vt, y, z; \alpha_C) = 0$ with the correction (Ref. 22), describing the bead shape in the process zone. Height and width of the bead as well as the coordinates of the solidification points on the top and at the edge of the bead are free parameters which have to be fitted to the temperature field

of a boundary element technique (BEM) in an iterative procedure, starting with certain assumptions about the bead geometry. The BEM is derived from the steady-state heat diffusion equation in a reference system moving with the speed $\vec{v}$ relative to the body:

$$-\rho_0 c\vec{v}\frac{\partial T}{\partial \vec{r}} - \frac{\partial}{\partial \vec{r}}\lambda\frac{\partial T}{\partial \vec{r}} = 0,$$

$$G_R(\vec{r}) = \frac{\exp\left[-\frac{|\vec{v}|\,|\vec{r}| + \vec{v}\cdot\vec{r}}{2a}\right]}{4\pi\lambda|\vec{r}|},$$

$$\text{(Eq 23)}$$

$$-\rho_0 c\vec{v}\cdot\frac{\partial G_R}{\partial \vec{r}} - \frac{\partial}{\partial \vec{r}}\lambda\frac{\partial G_R}{\partial \vec{r}} = \delta(\vec{r}).$$

Multiplying the first differential equation (Eq 23) with Rosenthal's solution $G_R(\vec{r} - \vec{r}')$ for a point source and integrating by parts over the whole domain consisting of substrate and bead yields

$$[T(\vec{r}) - T_U]\frac{\Omega(\vec{r})}{4\pi} - \lambda \iint\limits_{\text{workpiece surface}} d\vec{f}\,' \cdot \frac{\partial G_R(\vec{r} - \vec{r}')}{\partial \vec{r}}[T(\vec{r}') - T_U]$$

$$= - \iint\limits_{\text{workpiece surface}} d\vec{f}\,' \cdot \vec{q}_{ext}(\vec{r}')G_R(\vec{r} - \vec{r}').$$

$$\text{(Eq 24)}$$

Here $\Omega(\vec{r})$ is the local space angle under which the domain appears at the point $\vec{r}$, and

$$-\vec{n}\cdot\vec{q}_{ext} = \rho_0 c\vec{v}\cdot\vec{n}[T(\vec{r}) - T_U] + \lambda\vec{n}\cdot\frac{\partial T}{\partial \vec{r}} - \alpha[T(\vec{r}) - T_U]$$

$$= q_{particles} + q_{laser} + q_{losses}$$

$$\text{(Eq 25)}$$

is the local density of the external heat flux into the workpiece comprising the heat content of the powder particles resorbed at the liquid surface and the absorbed laser beam power as well as the energy losses by thermal radiation and convection cooling. $\vec{n}$ is the outward surface normal.

The integral equation (Eq 24) is transformed into a system of algebraic equations by discretizing the domain surface. Thereby the mesh is fitted well to the bead shape by using elliptical coordinates in the projection of the bead surface onto the substrate surface plane. Once the surface

temperatures have been determined, the bulk temperatures can be directly calculated from Eq 24.

Compared with finite element and finite difference methods this numerical technique needs only a two-dimensional mesh for computing a three-dimensional temperature field. It saves calculation time since only surface temperatures are needed during the iterations described below. On the other hand, it requires some care in calculating singular integrals.

The equivalent heat source distribution needed for the temperature field calculation comprises the terms q_{laser} and $q_{\text{particles}}$ of Eq 25. These terms are determined from the attenuated energy flux density distribution $j_E^*(x, y, Z(x, y))$ of the laser beam (see Eq 16) as well as from the mass flow $j^*[x, y, Z(x, y)]$ (see Eq 15) and the specific enthalpies $h_P[x, y, Z(x, y); R]$ of the resorbed particles that have been calculated as described in Section 4.1.2:

$$q_{\text{laser}} = -A \, \vec{n} \cdot \vec{j}_E^*[(x, y, Z(x, y))],$$

$$q_{\text{particles}} = -\vec{n} \cdot \vec{j}^*[(x, y, Z(x, y))] \Theta[T(x, y, Z(x, y)) - T_M]$$

$$\times \int_0^\infty dR \, w(R) \{ h_P[x, y, Z(x, y); R] - Q_P \}$$

$$\times \Theta[T_P(x, y, Z(x, y); R) - T_{\lim}], \quad \int_0^\infty dR \, w(R) = 1.$$

$$\text{(Eq 26)}$$

Thereby the latent heat of fusion, Q_P, of the powder particles is taken into account.

The Heaviside functions exclude particles that do not meet the melting zone or have temperatures T_P less than a limiting temperature $T_{\lim}$. An averaging procedure over the distribution $w(R)$ of particle radii may be required since the specific enthalpies and the temperatures of the preheated particles vary depending on their size.

Strictly speaking, the thermocapillary flow and the fluid flow caused by the momentum transfer by the impinging particles on the temperature field may influence the equivalent heat source. These effects are taken into account very crudely in the FEM model described below by using an enhanced value of the thermal conductivity of the fluid.

Simulating the bead-generation process, the temperature field is calculated first for the planar substrate and a single bead with a powder supply that is stepwise, increased up to the required value.

The temperature distribution obtained for a given bead depends on its shape and size and on the energy input, which means also on the resorbed powder mass and enthalpy. If too many particles and those that are too cold would be resorbed, the calculated melt pool temperature could fall even below the melting point. In reality, such excessive particles are not melted but transported to the melt pool border by the Marangoni flow. In the model, the only particles that are resorbed are at a temperature T_P that exceeds some limiting value $T_{\lim}$, which depends on the surface temperature and is properly fitted if necessary. The remainder of the particles are rejected. Hence, also the powder catchment and thus the size of melt pool and bead may be strongly influenced by changes of the temperature field.

Therefore, if the surface temperature distribution has been calculated for a given bead geometry, the shape and size of the bead have to be corrected according to the obtained molten area and the amount of resorbed powder. The temperature field is recalculated with these changes. This procedure has to be repeated several times until the conditions at the boundary of the molten part of the bead are fulfilled. Under-relaxation has to be used to get convergence.

Moreover, process parameters have to be adjusted during the iterations to provide the prescribed bead shape and a temperature distribution at the substrate-bead interface that yields the required strong metallurgical bond with minimum dilution. Then the required values of laser beam power and radius as well as of the powder rate are results of this procedure.

An example of temperature field and bead shape obtained in the described way is represented in Fig. 7, showing temperature distributions on selected surfaces and sections through the corresponding bead. Since in the given case the powder particles are not melted when arriving at the workpiece surface, the melt zone boundary is determined by the substrate melting temperature ($T_M = T_{MS}$). The process parameters have been determined to ensure that the substrate melting temperature of 1450 °C is only slightly exceeded at the substrate-coating interface in order to avoid bead dilution (see Fig. 7b).

4.2 FEM Model

The thermal stress history can be calculated by using a commercial finite element code if the actual workpiece geometry and the equivalent heat source distribution are known. Therefore the initially inactive elements of the bead are activated at that front at which the bead is generated in reality, that means at the moving melt pool surface (Fig. 6 or 8) calculated before. This activation is performed as a phase transition from a virtual initial phase having extremely low values of specific heat and Young's modulus, which ensures that no action can be exerted on the real workpiece by the inactive elements.

Heat input at the front mentioned has to be described by a body source within a thin transition layer instead of a surface source since the front is running through the body-fixed mesh, thereby crossing and activating its elements. The layer thickness η has to be small compared with the bead height but should comprise at least about three elements. This layer fits to the precalculated shape of the melt pool surface described by the function in Eq 20 and 22, whereas the projection of the power density distribution onto the x-y plane, $q_2(x-vt, y)$, is derived from the equivalent heat source (Eq 26). From a physical viewpoint, the transition layer represents that zone where the impinging particles dissolve and cause some mixing effect by local microconvection.
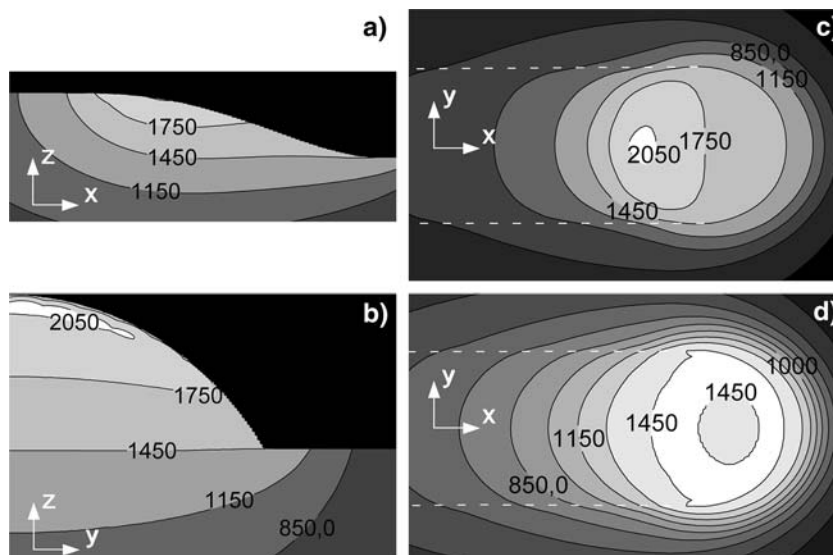
Having solved Eq 20 for z:

Fig. 7 Calculated temperature field in the process zone in laser cladding. (a) Isotherms (temperature values in °C) on a longitudinal section in the symmetry plane of the bead. (b) Local maximum temperatures in degrees centigrade on a cross section through the bead. (c) Isotherms of the temperature distribution on the surface of the bead (bounded by the 1450 °C isotherm at its front side and by the white dashed lines else) and the surrounding substrate surface. (d) Temperature distribution on the substrate-coating interface inside the bead (bounded as in Fig. 7c) and the substrate surface outside the bead
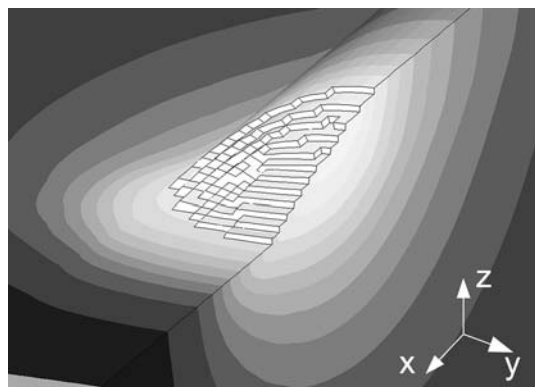
Fig. 8 Just activated bead elements in the process zone and temperature distribution on the surfaces of bead and substrate and on a longitudinal section in the bead symmetry plane (at the right-hand side)

$$f(x, y, z; \alpha_C) = 0 \, nbsp; \rightarrow nbsp; z = Z(x,y;\alpha_C) \, \Theta[Z(x,y;\alpha_C)] \tag{Eq 27}$$

the spatial power density distribution to be implemented into the FEM code may be written as

$$q(x - vt, y, z) = 2 \, \frac{q_2(x - vt, y)}{\sqrt{\pi}\eta} \exp\left\{ -\frac{[Z(x - vt, y; \alpha_C) - z]^2}{\eta^2} \right\}$$
$$\times \, \Theta[Z(x - vt, y; \alpha_C) - z]. \tag{Eq 28}$$

Here Heaviside's step function $\Theta[Z(x - vt, y; \alpha_C) - z]$ ensures that heat is absorbed only in active cells below the actual surface. A special capability of the FEM code is

used to check whether the heat input into the body really achieved the required value.

In the first step the FEM code calculates the temperature field once more, now taking into account even nonlinear effects such as temperature-dependent material properties and latent heats. At the same time, the phase transformations in the substrate are simulated using kinetic equations. All the phase transformations, that means the activation of cells at the melt pool surface as well as the formation of austenite during heating and the transformation to ferrite/pearlite, bainite, or martensite during cooling, are described by means of a user-defined FORTRAN program coupled to the finite element code via an existing interface. The distribution of thermometallurgical strain and the yield stress are derived that determine the resulting thermal stress from both the tempetature field and the phase volume fractions.

For the subsequent stress calculation, an elastic-plastic material behavior with isotropic strain hardening was assumed. Flow curves for the investigated coatings (Stellite 21 and Stellite 20) have been obtained by means of hot tensile tests using a Gleeble apparatus. Any reverse actions of the mechanical process on the thermometallurgical history (dissipated strain energy, stress-induced phase transformations) are neglected.

Additional heat sources may be used to reduce the danger of cracking by means of preweld or postweld heating. The required heat input can be performed advantageously using electromagnetic inductors, which may be directly integrated into the technological process of laser cladding. The external alternating magnetic field creates eddy currents and Joule's heat in a surface layer of thickness δ, which depends on the circular frequency ω of

the alternating current, the electrical resistivity ρ, and the magnetic permeability μ of the material:

$$\delta = \sqrt{\frac{2\rho}{\mu_0\mu\omega}}, \quad \mu_0 = 4\pi \; 10^{-10} \; \frac{Vs}{Amm}. \tag{Eq 29}$$

Strictly speaking, the eddy current density distribution and the heat input had to be determined by solving Maxwell's equations numerically. However, for a sufficiently thick workpiece with a planar surface the mean Joule's heat power density distribution generated by a uniformly moving inductor may be approximately described by:

$$q_I(x - vt, y, z) = \frac{q_{2I}(x - vt, y)}{\delta} \exp\left(-\frac{|z|}{\delta}\right). \tag{Eq 30}$$

The two-dimensional power density q_{2I} $(x - vt, y)$ depends on the shape of the inductor.

The electrical resistivity ρ, the magnetic permeability μ, and the electromagnetic penetration depth δ sensitively depend on the temperature. In ferromagnetic materials, δ may increase by about 1 order of magnitude when the permeability is reduced to unity above the Curie point. To account for this effect, the quantity $\delta \rightarrow \delta[T(x - vt, y, z)]$ is considered as a function of temperature in Eq 30. For frequencies of about 10 kHz and more, however, this correction does not significantly increase the effective penetration depth of heat since even at high temperatures the electromagnetic penetration depth δ is usually much smaller than the heat diffusion length $\sqrt{2a\Delta t_i}$, where Δt_i is the time of inductive heating and a the heat diffusivity.

5. Temperature Distribution, Phase Fractions, and Stress Field at a Single Bead

Using the finite element model just described, the following results were obtained for the laser cladding of a Stellite 21 coating on the steel Ck45 (Fig. 9).

Figures 9(a) and (c) show the steady-state temperature field in the symmetry plane of the process zone and the evolution of phase volume fractions along the white dotted line in Fig. 9(a), respectively. Figure 9(b) gives the pattern of transverse stress within the same plane, which may be understood as follows.

In front of the process zone, rising temperatures lead to the formation of compressive stresses, which afterwards are reduced by plastic flow to very low values in the strongly heated region. The initially fused weld bead material is free of stress. During subsequent cooling, thermal contraction causes tensile stresses in the solidified coating and in the plastic zone (compare regions 3 and 4 in Fig. 2c). Plastic flow prevents these cooling stresses from exceeding the corresponding yield stress in the coating and immediately below. Enhanced plastic flow during cooling in the austenitic state and volume expansion due to the formation of martensite during further cooling may lead to a stress reversal and finally to compressive stress in a layer below the substrate/coating interface. For reasons of

equilibrium, this effect still increases the tensile stress in the adjacent regions within the coating and below the layer with the martensite. This is exactly the same explanation as that used for the results shown in Fig. 2(c). Thus it is not surprising that the course of stress along the vertical dashed line in Fig. 9(b), where the final state has been almost achieved, is very similar to that shown in Fig. 2(c) for the residual stress in the one-dimensional model.

The longitudinal stress shown in Fig. 9(d) is generally much larger than the transverse stress (Fig. 9b) since the "clamping conditions" for the considered volume element are much more rigid along the bead direction than across it. Otherwise the stress pattern is similar for both components.

During the generation of long straight beads a steady-state arises, and the resulting stress state becomes independent of the coordinate x along the bead direction. This state is achieved at the right-hand side of Fig. 9(b) and (d). Deviations from this state occur at the ends of the bead. Figure 10 shows calculated distributions of the transverse stress σ_{yy} and the longitudinal stress σ_{xx} for both cases. Therefore, it is important whether the bead ends close to (1) or far from (2), the substrate boundary. It is noteworthy that in the latter case the stresses are much larger near to the bead end than in the middle part of the bead, probably because of the higher cooling rates that occur after the laser has been shut off. At the substrate boundary, the represented stresses are reduced owing to the enhanced possibilities of relaxation at the stress-free boundary. Correspondingly stronger distortion is found in this region. Such effects have to be considered when choosing the bead pattern for an optimized coating strategy.

As already explained in detail in Section 3.4, the coating stress decreases with increasing heating time (see Fig. 3a). This result obtained with the one-dimensional model is confirmed by the numerical three-dimensional stress calculations shown in Fig. 11(a): With increasing feed rate the transverse (and also the longitudinal) stress become larger.

Figure 11(b) shows that the transverse stress increases with the bead width since the possibilities of relaxation decrease.

6. Stress Reduction by Preheating or Postweld Heating

High crack susceptibilities and large residual stresses in hard coatings are still a serious problem. As already mentioned in Section 3.4, they can be reduced by preheating or postweld heating. The main idea is to reduce the thermal strain difference between coating and substrate and to facilitate heat equalization at relatively high temperatures at which most materials undergo plastic deformation rather than brittle fracture. Furthermore, substrate hardening and the resulting reaction stress in the coating may be avoided in this way.
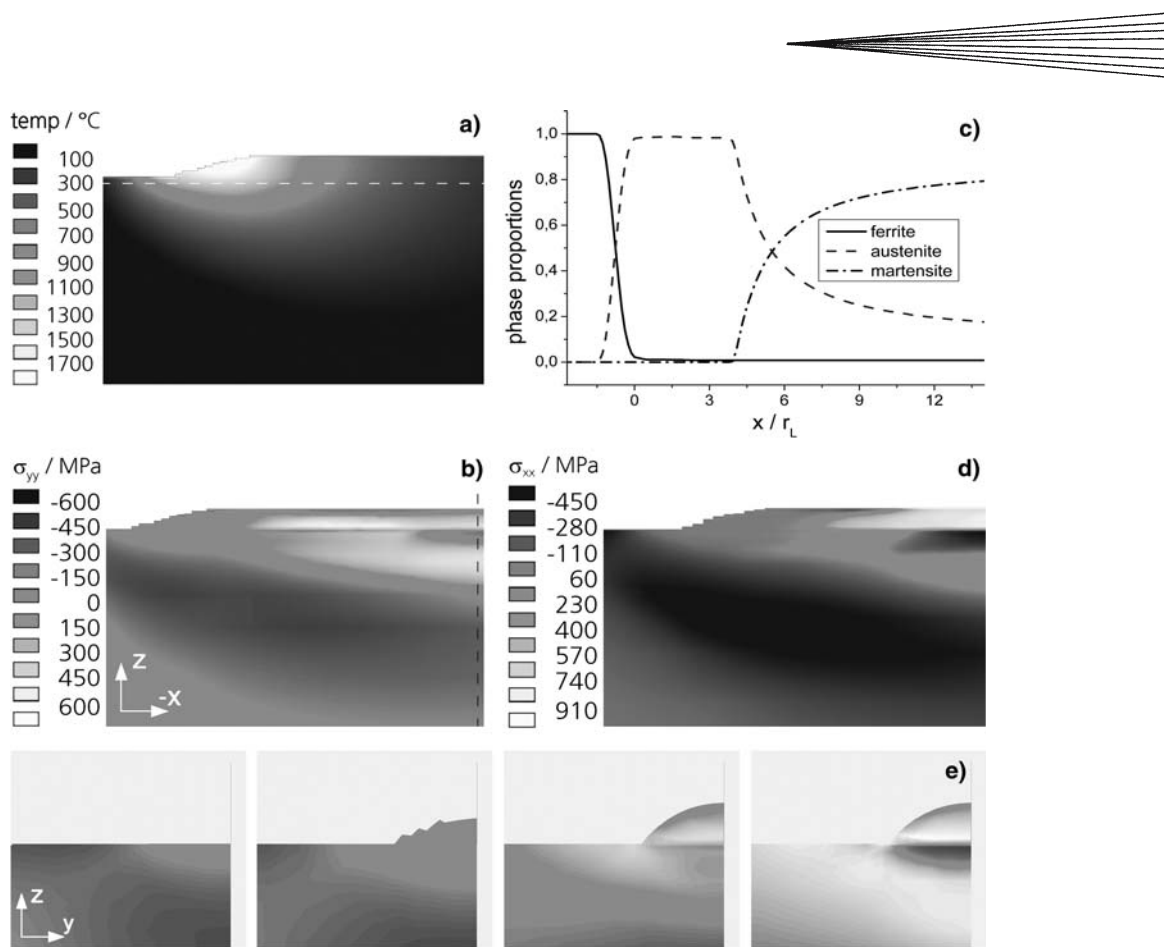
Fig. 9 Evolution of temperature field, phase proportions, and stress field for a stellite 21 coating on steel Ck45. (a) Temperature distribution in the symmetry plane of the bead. (b) Transverse stress distribution in the same range of the bead's symmetry plane as in Fig. 9(a). The vertical dashed line at the right-hand side of the figure may be used for a comparison with Fig. 2(c). (c) Evolution of phase volume fractions along the white dashed line in Fig. 9(a). r_L is the laser beam radius. The position $x = 0$ corresponds to the laser beam center. (d) Longitudinal stress distribution on the symmetry plane of the bead. (e) Evolution of the bead and the transverse stress on a cross section perpendicular to the feed direction
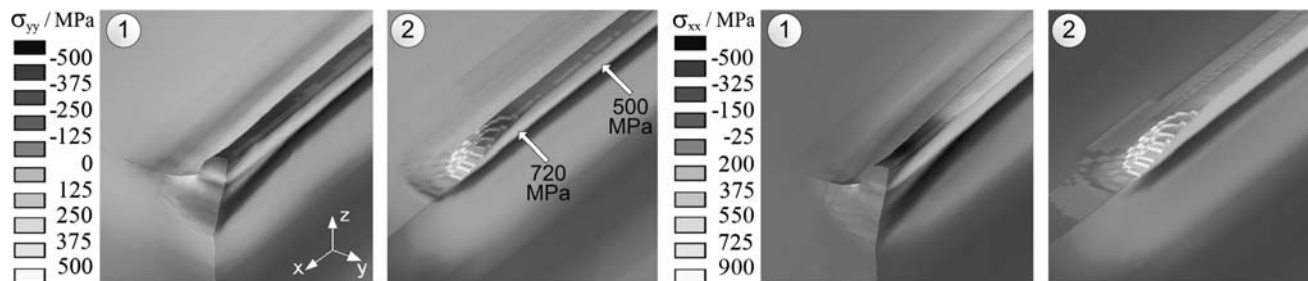

Fig. 10 Transverse and longitudinal stress components, σ_{yy} and σ_{xx}, at the bead end for the two cases, where the bead ends at the stress-free substrate boundary (1) or in the middle part of the substrate plane (2). For obviousness, the represented distortion has been enlarged by a factor of 20

Preheating of the entire workpiece in a furnace is best suited to reduce stress but hardly may be integrated into a technological process. Brenner et al. (Ref 54-57) succeeded in the crack-free generation of coatings made from such hard materials as, for example, Deloro 60 on heat treatable steels and cold work steels by preheating the process zone using an inductor connected with the moving laser head. Therefore frequencies around 10 kHz were

found to be very efficient irrespective of the comparatively strong skin effect that restricts the penetration depth of Joule's heat to values less than about 1 mm in ferromagnetic materials.

In the present work stress calculations have been performed for the laser cladding (Stellite 21 on steels C15 and Ck45) with inductive preweld and postweld heating to investigate the influence of the process parameters on the
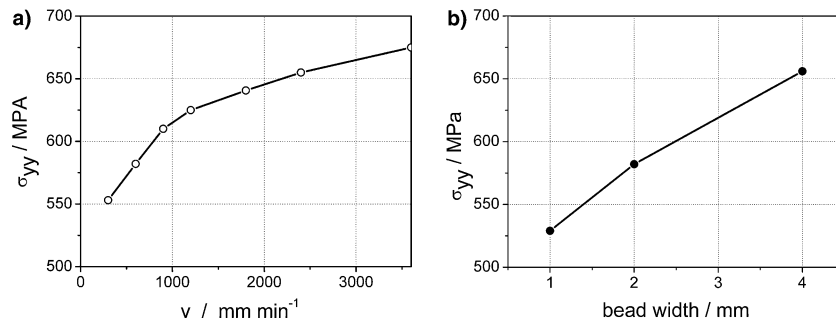
Fig. 11 Dependence of the transverse stress in the coating on feed rate (a) and bead width (b) for a fixed aspect ratio (width:height = 4)
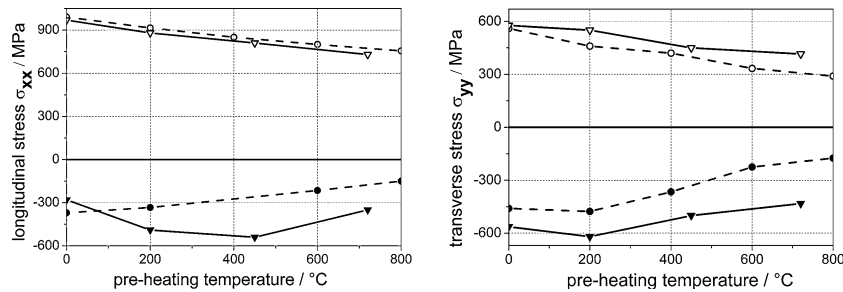

Fig. 12 Maximum transverse (σ_{yy}) and longitudinal (σ_{xx}) stresses across a bead as functions of the preheating temperature in a furnace for a 2 mm wide single bead (feed rate: 600 mm/min). The maximum tensile and compressive stresses occur in the coating and in the substrate, respectively. The solid lines refer to a Stellite 21 coating on steel Ck45, the dashed lines to Stellite 21 on steel C15
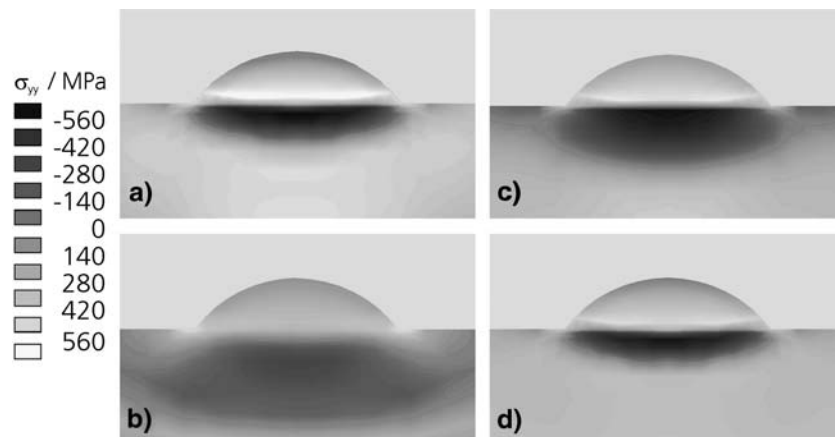

Fig. 13 Transverse stress σ_{yy} across a bead with and without preweld or postweld heating up to 700 °C (bead width w = 2 mm, feed rate v = 600 mm/min): (a) Stress pattern after laser cladding without any additional heat sources. (b) Stress reduction by preheating in a furnace. (c) Inductive preheating (inductor diameter: 40 mm). (d) Inductive postweld heating (inductor diameter: 40 mm)

achieved reduction of transverse and longitudinal stresses in a single bead.

The inductor should be arranged as closely as possible to the process zone to avoid too low a minimum temperature between the two heat sources. If the inductor size is enlarged, the cooling rate decreases for a fixed preheating temperature but the required heat input increases. Thus there is an optimum size that has to be determined. Besides, the efficiency of preweld and postweld heating is compared.

Figure 12 shows the influence of the preheating temperature in a furnace on the maximum tensile and compressive stresses in coating and substrate, respectively. Here the effect of preheating appears slightly more pronounced than in the one-dimensional model (Fig. 3b). This might be due to the suppression of hardening that was not essential in the latter.

A comparison of stress reduction by preheating in the furnace, inductive preheating, and inductive postweld heating is given in Fig. 13. As expected because of the
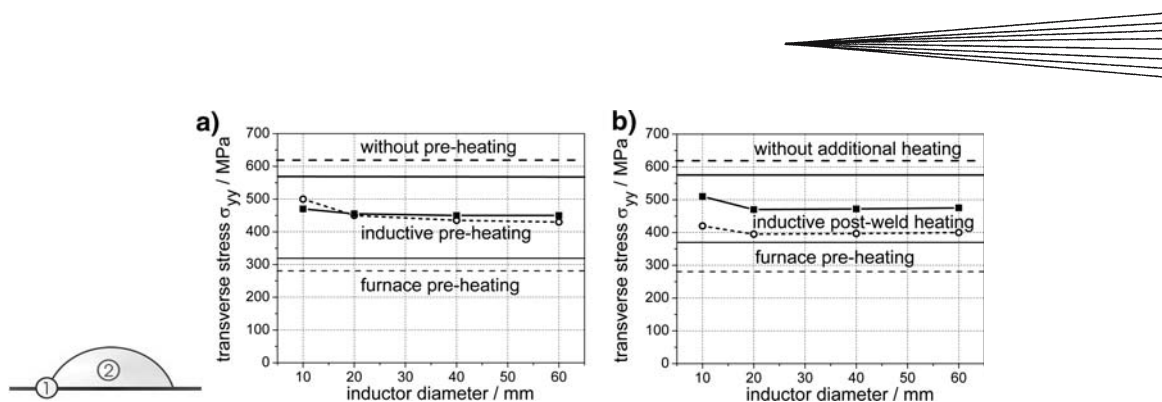
Fig. 14 Maximum transverse stress at positions (1) (dashed lines) and (2) (solid lines) in the bead, after inductive preweld or postweld heating up to 700 °C, as functions of the diameter of a circular inductor in comparison with values achieved by furnace preheating or without additional heating (bead width: 2 mm, feed rate: 600 mm/min). (a) Inductive preheating (Stellite 21 on steel C15). (b) Inductive postweld heating (Stellite 21 on steel Ck45)
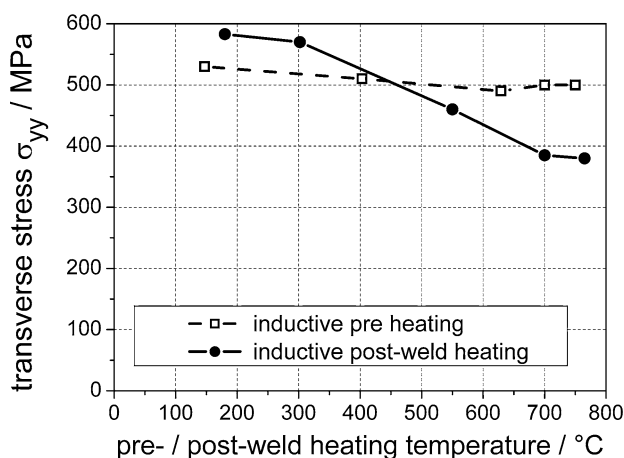

Fig. 15 Influence of preweld and postweld heating temperatures on the maximum transverse stress σ_{yy} in a stellite 21 coating on steel Ck45

limited heat penetration depth, the local preheating by the inductor is not as efficient as preheating in the furnace. The latter, however, is not feasible for most applications. Increasing the inductor size reduces lateral heat conduction losses but only slightly increases the heat penetration depth, since the heat diffusion length is proportional to the square root of the heating time. For that reason, increasing the inductor diameter beyond 20 mm could not significantly improve the results obtained for a feed rate of 600 mm/min and a preheating temperature of 700 °C, as it is shown in Fig. 14.

Figure 15 visualizes the dependence of the residual transverse stress in the coating on the maximum local temperature achieved by the additional heat source. At first sight, inductive postweld heating seems to yield better results than preheating. However, further investigations are required to confirm this result and to clarify the reasons for it.

7. Conclusions

The intention of the present work is to find variants of processing that are suited to reduce residual stresses and

the danger of cracking even in very hard coatings generated by laser cladding. An analytical one-dimensional model was used to visualize the essential phenomena that influence the evolution of residual stress and strain in the laser cladding process. It shows the significant role of phase transformations and plastic deformation and the influence of parameters such as heating time and preheating temperature in a furnace on residual stress and distortion.

As a rule, cracking in a thin, homogeneous elastic-plastic coating is expected to occur only after strong strain hardening, since triaxial stress states with a large hydrostatic part are unlikely to form in a sufficiently thin coating at the stress-free surface. However, very large plastic strain of more than 2% may have been cumulated in the coating after cooling. This value significantly exceeds the fracture strain of a series of coating materials such as Stellite 20, SF6 and so forth and thus may give rise to the formation of cracks. Preheating or postweld heating using inductive heat sources are possibilities to force the heat, which has been brought into the material by the cladding process, to equalize on a relatively high temperature level where stresses are reduced by plastic flow without strong strain hardening. Stresses may still increase during further cooling when the coating contracts more strongly than the substrate, but fracture stress is unlikely to be achieved at this stage. Moreover, preweld or postweld heating are suited to suppress substrate hardening that otherwise would increase the tensile stresses in the coating.

As a basis of farther-reaching stress calculations using of a finite element code a process model of laser cladding has been developed that considers the interaction of the powder jet and the laser beam, substrate heating and melting, and heat losses by conduction, reflection, convection, thermal radiation, and evaporation, as well as the powder resorption by the melt pool, yielding the bead geometry and the related temperature field in the process zone.

Using these results, three-dimensional transient stress calculations have been carried out at a single bead to investigate the influence of process parameters and especially of preweld and postweld heating on stress evolution and residual stress. Inductive preweld or postweld heating

were found to yield a distinct stress reduction. An optimum inductor size of 20 mm was determined for a 2 mm wide bead of Stellite 21 on steel Ck45, a feed rate of 600 mm/min, and a maximum preheating temperature of 700 °C. Studies on other materials and sets of parameters will follow.

Up to now, our model has been applied to single beads only. Further work is in progress to verify the results by experiments and to include overlapping beads forming closed coatings and various bead patterns as well as to estimate the stresses for coatings or three-dimensional parts that consist of several layers.

Acknowledgment

References

1. V.M. Weerasinghe and W.M. Steen, Computer Simulation Model for Laser Cladding, *ASME H.T.D.*, 1983, **29**, p 15-23
2. L. Li, W.M. Steen, and R.B. Hibberd, Computer Aided Laser Cladding, *Proc. ECLAT'90*, H.W. Bergmann and R. Kupfer, Ed., Sept 1990 (Erlangen, Germany), Arbeitsgemeinschaft Wärmebehandlung und Werkstofftechnik e.V. (AWT), 1990, Vol 1, p 355-369
3. C.F. Marsden, A. Frenk, J.-D. Wagnière, and R. Dekumbis, Effects of Injection Geometry on Laser Cladding, *Proc. ECLAT'90*, H.W. Bergmann and R. Kupfer, Sept 1990 (Erlangen, Germany), Arbeitsgemeinschaft Wärmebehandlung und Werkstofftechnik e.V. (AWT), 1990, Vol 1, p 535-542
4. C.F. Marsden, A.F.A. Houdley, and J.-D. Wagnière, Characterisation of the Laser Cladding Process, *Proc. ECLAT'90*, H.W. Bergmann and R. Kupfer, Ed., Sept 1990 (Erlangen, Germany), Arbeitsgemeinschaft Wärmebehandlung und Werkstofftechnik e.V. (AWT), 1990, **1**, p 543-553
5. C.F. Marsden, A. Frenk, and J.-D. Wagnière, Power Absorption During the Laser Cladding Process, *Laser Treatment of Materials—Proc. ECLAT'92*, B.L. Mordike, Ed., Sept 1992 (Göttingen), DGM-Informationsgesellschaft Verlag, 1992, p 375-380
6. W.-B. Li, H. Engström, J. Powell, Z. Tan, and C. Magnusson, Modelling of the Laser Cladding Process—Preheating of the Blown Powder Material, *Lasers Eng.*, 1995, **4**, p 329-341
7. H. Gedda, W.-B. Li, H. Engström, C. Magnusson, J. Powell, and G. Wahlström, Energy Redistribution During CO_2 Laser Cladding, *Proc. Laser Materials Processing Conference ICALEO 2001*, Oct 2001 (Jacksonville, FL), 2001, p 701
8. J. Lin, Temperature Analysis of the Powder Streams in Coaxial Laser Cladding, *Optics Laser Technol.*, 1999, **31**, p 565-570
9. J. Lin and B.-C. Hwang, Coaxial Laser Cladding on an Inclined Substrate, *Optics Laser Technol.*, 1999, **31**, p 571-578
10. J. Lin, A Simple Model of Powder Catchment in Coaxial Laser Cladding, *Optics Laser Technol.*, 1999, **31**(3), p 233-238
11. J. Lin and B.-C. Hwang, Clad Profiles in Edge Welding Using a Coaxial Powder Filler Nozzle, *Optics Laser Technol.*, 2001, **33**, p 267-275
12. C.-Y. Liu and J. Lin, Thermal Processes of a Powder Particle in Coaxial Laser Cladding, *Optics Laser Technol.*, 2003, **35**(2), p 81-86
13. T. Yoshida and K. Akashi, Particle Heating in a Radio-Frequency Plasma Torch, *J. Appl. Phys.*, 1977, **48**(6), p 2252-2260
14. A.F.A. Hoadley and M. Rappaz, A Thermal Model of Laser Cladding by Powder Injection, *Metall. Trans. B*, 1992, **23B**(5), p 631-642
15. M. Picasso and A.F.A. Hoadley, Finite Element Simulation of Laser Surface Treatments Including Convection in the Melt Pool, *Int. J. Num. Meth. Heat Fluid Flow*, 1994, **4**, p 61-83
16. N. Pirch, E.W. Kreutz, L. Möller, A. Gasser, and K. Wissenbach, Melt Dynamics in Surface Processing with Laser Irradiation, Proc. ECLAT'90, H.W. Bergmann and R. Kupfer, Ed., Sept 1990 (Erlangen, Germany), Arbeitsgemeinschaft Wärmebehandlung und Werkstofftechnik e.V. (AWT), 1990, p 65-80
17. B. Ollier, N. Pirch, E.W. Kreutz, and H. Schlüter, Cladding with Laser Radiation: Properties and Analysis, Laser Treatment of Materials—Proc. ECLAT'92, B.L. Mordike, Ed., DGM—Informationsgesellschaft Verlag, 1992, p 687-692
18. B. Ollier, N. Pirch, and E.W. Kreutz, Ein numerisches Modell zum einstufigen Laserstrahlbeschichten (A Numerical Model of Single-Stage Laser Cladding), *Laser und Optoelektronik*, 1995, **27**(1), p 63-70, (in German)
19. H. Schmitter, "Simulation des einstufigen Laserbeschichtens mit FIDAP" (Simulation of the Single-Stage Laser Cladding), student research project, IFSW Stuttgart, 1994 (in German)
20. M. Picasso, C.F. Marsden, J.-D. Wagniere, A. Frenk, and M. Rappaz, A Simple but Realistic Model for Laser Cladding, *Metall. Mater. Trans. B*, 1994, **25B**, p 281-291
21. A.F.H. Kaplan and G. Groboth, Process Analysis of Laser Beam Cladding, *J. Manuf. Sci. Eng.*, 2001, **123**, p 609-614
22. D. Lepski, H. Eichler, V. Fux, S. Scharek, and E. Beyer, Calculating Temperature Field and Single Track Bead Shape in Laser Cladding with Marangoni Flow using Rosenthal's Solution, *Lasers in Manufacturing—Proc. First Int. WLT-Conference on Lasers in Manufacturing*, Wissenschaftliche Gesellschaft Lasertechnik e.V. (WLT), June 2001 (Munich), 2001, p 167-177
23. D. Lepski, H. Eichler, V. Fux, S. Scharek, and E. Beyer, Simulation of the Powder Injection Laser Beam Cladding Process, *Proc. Internat. Conf. "THE" Coatings in Manufacturing Engineering and EUREKA Partnering Event*, Nov 2002 (Thessaloniki, Greece), 2002, p 529-538
24. D. Lepski, H. Eichler, S. Scharek, V. Fux, E. Zoestbergen, and E. Beyer, Simulation Software for Laser Beam Cladding in Manufacturing, *Proc. 16th Meeting on Mathematical Modeling of Materials Processing with Lasers* (M^4PL16), Jan 2003 (Igls, Austria)
25. D. Lepski, H. Eichler, S. Scharek, V. Fux, St. Nowotny, and E. Beyer, Simulation of Laser Beam Cladding by Powder Injection, *Int. Conf. Laser 2003—World of Photonics*, June 2003 (Munich), 2003
26. N. Pirch, S. Mokadem, S. Keutgen, K. Wissenbach, and E.W. Kreutz, 3D-Model for Laser Cladding by Powder Injection, *Laser Assisted Net Shape Engineering 4, Proc. LANE 2004*, M. Geiger and A. Otto, Ed., Sept 2004 (Erlangen, Germany), 2004, p 851-858
27. E. Toyserkani, A. Khajepour, and S. Corbin, 3-D Finite Element Modeling of Laser Cladding by Powder Injection: Effects of Laser Pulse Shaping on the Process, *Opt. Lasers Eng.*, 2004, **41**, p 849-867
28. J. Ahlström, B. Karlsson, and S. Niederhauser, Modeling of Laser Cladding of Medium Carbon Steel—a First Approach, *J. Phys. IV France*, 2004, **120**, p 405-412
29. L. Han, F.W. Liou, and K.M. Phatak, Modeling of Laser Cladding with Powder Injection, *Metall. Mater. Trans. B*, 2004, **35**, p 1139-1150
30. L. Han, K.M. Phatak, and F.W. Liou, Modeling of Laser Deposition and Repair Process, *J. Laser Appl.*, 2005, **17**(2), p 89-99
31. J. Choi, L. Han, and Y. Hua, Modeling and Experiments of Laser Cladding with Droplet Injection, *Trans. ASME*, 2005, **127**, p 978-986
32. R.K. Chin, J.L. Beuth, and C.H. Amon, Thermomechanical Modelling of Successive Material Deposition in Layered Manufacturing, *Proc. Solid Freeform Fabrication Symposium*, 1996 (Austin, TX), 1996, p 507-514
33. R.K. Chin, "Thermomechanical Modelling of Residual Stresses in Layered Manufacturing with Metals", Ph.D. Thesis, Carnegie Mellon University, 1998
34. N.W. Klingbeil, "Residual Stress Induced Warping and Interlayer Debonding in Layered Manufacturing", Ph.D. Thesis, Carnegie Mellon University, 1998

35. N.W. Klingbeil, J.L. Beuth, R.K. Chin, and C.H. Amon, Measurement and Modelling of Residual Stress-Induced Warpage in Direct Metal Deposition Processes, Proc. Solid Freeform Fabrication Symposium, 1998 (Austin, TX), 1998, p 367-374

36. A.M. de Deus and J. Mazumder, Two-Dimensional Thermo-Mechanical Finite Element Model for Laser Cladding, *Proc. ICALEO*, 1996 (Detroit, MI), 1996, p 174-183

37. A.M. de Deus, ''A Thermal and Mechanical Model of Laser Cladding'', PH.D. Thesis, University of Illinois, 2004

38. A.H. Nickel, ''Analysis of Thermal Stresses in Shape Deposition Manufacturing of Metal Parts'', Ph.D. Thesis, Stanford University, 1999

39. A.H. Nickel, D.M. Barnett, and F.B. Prinz, Thermal Stresses and Deposition Patterns in Layered Manufacturing, *Mater. Sci. Eng.*, 2001, **A317**, p 59-64

40. F.-J. Kahlen and A. Kar, Residual Stresses in Laser-Deposited Metal Parts, *J. Laser Appl.*, 2001, **13**(12), p 60-69

41. K. Dai and L. Shaw, Thermal and Stress Modeling of Multi-Material Laser Processing, *Acta Mater.*, 2001, **49**, p 4171-4181

42. S. Ghosh and J. Choi, Three-Dimensional Transient Residual Stress Finite Element Analysis for Laser Aided Direct Metal Deposition Process, *Proc. ICALEO 2003*, 2003 (Orlando, FL), CD-Rom No. 908

43. S. Ghosh and J. Choi, Three-Dimensional Transient Finite Element Analysis for Residual Stresses in the Laser Aided Direct Metal/Material Deposition Process, *J. Laser Appl.*, 2005, **17**(3), p 144-158

44. R. Jendrzejewski, G. Sliwinski, M. Krawczuk, and W. Ostachowicz, Temperature and Stress Fields Induced During Laser Cladding, *Comput. Struct.*, 2004, **82**, p 653-658

45. R. Jendrzejewski, I. Kreja, and G. Sliwinski, Temperature Distribution in Laser-Clad Multi-Layers, *Mater. Sci. Eng.*, 2004, **A379**, p 313-320

46. R. Jendrzejewski, G. Sliwinski, M. Krawczuk, and W. Ostachowicz, Laser Cladding of Protective Coatings of Limited Cracking Susceptibility, XV. *International Symposium on Gas Flow, Chemical Lasers, and High-Power Lasers*, J. Kodymová, Ed., Aug-Sept 2004 (Prague, Czech Republic), 2004, p 925-928

47. A. Plati, J.C. Tan, I.O. Golosnoy, R. Persoons, K. van Acker, and T.W. Clyne, Residual Stress Generation During Laser Cladding of Steel with a Particulate Metal Matrix Composite, *Adv. Eng. Mats.*, Jan 2006, **8**(7), p 619-624

48. Y. Zhang, Z. Xianghua, and Y. Xiangkai, Elimination of Laser Cladding Cracks: Thermal Control and Stress Analysis, *Proc. ICALEO 2001*, 2001 (Orlando, FL), 2001, p 705

49. G.W. Greenwood and R.H. Johnson, The Deformation of Metals Under Small Stresses During Phase Transformations, *Proc. R. Soc. London. Series A, Math. Phys. Sci.*, 1965, **283**(1394), p 403-422

50. J.-B. Leblond, G. Mottet, and J.C. Devaux, A Theoretical and Numerical Approach to the Plastic Behaviour of Steels During Phase Transformations, I: Derivation of General Relations, *J. Mech. Phys. Solids*, 1986, **34**(4), p 395-409

51. J.-B. Leblond, G. Mottet, and J.C. Devaux, A Theoretical and Numerical Approach to the Plastic Behaviour of Steels During Phase Transformations, II: Study of Classical Plasticity for Ideal Plastic Phases, *J. Mech. Phys. Solids*, 1986, **34**(4), p 411-432

52. J.-B. Leblond, J. Devaux, and J.C. Devaux, Mathematical Modelling of Transformation Plasticity in Steels, I: Case of Ideal Plastic Phases, *Int. J. Plast.*, 1989, **5**, p 551-572

53. J.-B. Leblond, J. Devaux, and J.C. Devaux, Mathematical Modelling of Transformation Plasticity in Steels, II: Coupling with Strain Hardening Phenomena, *Int. J. Plast.*, 1989, **5**, p 573-591

54. B. Brenner, V. Fux, A. Wetzig, and St. Nowotny, Induktiv unterstütztes Laserauftragschweißen-eine Hybridtechnologie überwindet Anwendungsgrenzen (Induction Assisted Laser Cladding-a Hybrid Technology Expands Limits of Application), *Proc. Sixth European Conference on Laser Treatment of Materials ECLAT'96*, Sept 16-18, 1996 (Stuttgart(D)), 1996, **1**, p 469-476 (in German)

55. B. Brenner, V. Fux, and A. Wetzig, Induktiv unterstütztes Laserauftragschweißen (Induction Assisted Laser Cladding), *Härt.-Tech. Mitt.*, 1997, **52**(4), p 221-225

56. B. Brenner and V. Fux, Induktiv unterstütztes Laserauftragschweißen—ein neues Verfahren zur effektiven Erzeugung hochverschleißbeständiger Randschichten (Induction Assisted Laser Cladding—A New Technology for the Efficient Generation of Highly Wear Protective Coatings), *Stahl*, 1999, p 48-50 (in German)

57. V. Fux and B. Brenner, Leistungsfähige Beschichtungsprozesse durch induktiv unterstütztes Laserauftragschweißen (High Performance Coating Technologies by Induction Assisted Laser Cladding), *Freiberger Forschungshefte*, 1999, **B297**, p 121-130, (in German)